Molecular beam epitaxy and crystal structure of majority *a*-plane-oriented and substrate-strained Mn₃Sn thin films grown directly on sapphire (0001)

Sneha Upadhyay,[1] Tyler Erickson,[1] Hannah Hall,[1] Ashok Shrestha,[1] David C. Ingram,[1] Kai Sun,[2] Juan Carlos Moreno Hernandez,[3] Gregorio Hernandez Cocoletzi,[3] Noboru Takeuchi,[4] and Arthur R. Smith[1]

AFFILIATIONS

[1] Nanoscale and Quantum Phenomena Institute, Department of Physics and Astronomy, Ohio University, Athens, Ohio 45701
[2] Michigan Center for Materials Characterization (MCMC) & Department of Materials Science and Engineering,
The University of Michigan, Ann Arbor, Michigan 48109
[3] Universidad Autónoma de Puebla, Instituto de Física, Apartado Postal J-48, Puebla 72570, Mexico
[4] Centro de Nanociencias y Nanotecnología, Universidad Nacional Autónoma de Mexico, Apartado Postal 14, Código Postal,
Ensenada, Baja California 22800, Mexico

ABSTRACT

The Kagome antiferromagnet Mn₃Sn has garnered much attention due to the presence of exciting properties such as anomalous Hall and Nernst effects. This paper discusses the synthesis of crystalline Mn₃Sn thin films, prepared on Al₂O₃ (0001) substrates at $453 \pm 5\,^\circ\mathrm{C}$ using molecular beam epitaxy. The growth is monitored *in situ* using reflection high energy electron diffraction and measured *ex situ* using x-ray diffraction, Rutherford back-scattering, and cross-sectional scanning transmission electron microscopy. Our analysis shows the *in-plane* lattice constants of $a_{1,M} = 4.117 \pm 0.027\,\text{Å}$ and $a_{2,M} = 4.943 \pm 0.033\,\text{Å}$, which is a very unexpected result when compared to the bulk *a*-plane Mn₃Sn. This indicates a strain in the film and makes it challenging to provide a straightforward explanation. In an effort to explain our results, we discuss two possible orientation relationships between the Mn₃Sn films and the sapphire substrates. Samples prepared under these conditions appear to have smooth surfaces locally, but overall the film has a 3D island morphology. First-principles calculations provide atomic models of the Mn₃Sn (11$\bar{2}$0) lattice on Al₂O₃ (0001) high symmetry sites, indicating that the L3-R90° is the most stable configuration. A detailed discussion of the experimental data and theoretical results, as well as strain effects, is provided.

I. INTRODUCTION

Antiferromagnets have gained much attention as materials for spintronic devices since they are expected to provide higher storage densities and faster operating speeds compared to ferromagnets.[1] One such material is Mn₃Sn, a non-collinear antiferromagnet that has shown a large anomalous Hall effect (AHE) below the Néel temperature of 430 K.[2–4] Furthermore, Mn₃Sn has other advantages such as zero stray field, high precession frequency, and small damping coefficient.[2,5] Using these materials for specific applications requires fabricating high-quality thin films.

In Fig. 1(a), we show the reproduced 3D crystal model of Mn₃Sn which indicates the *c*-plane by a green parallelogram and orthogonal cut (shown in yellow color) leading to an *a*-plane lattice. Figure 1(b) shows the *c*-plane Mn₃Sn hexagonal structure consisting of a Kagome lattice of Mn- and Sn-atoms in an ABAB stacking sequence. Three Mn-atoms form a triangular sub-lattice, with their magnetic moments lying in the *c*- (0001) plane with a 120-degree-spin order.[6] The reported lattice constants are a = 5.665 Å and c = 4.531 Å.[7]

Figure 1(c) shows the rectangular *a*-plane lattice with a 2-atom basis in which atom 1 is at the corner (0,0) and atom 2 is at $\left(\frac{1}{2}, \frac{2}{3}\right)$. Bulk-like unit cells are shown in the model including a 1×1 unit cell for the Mn layer, indicated by the solid orange rectangle, which has a bulk-like (unstrained) size with $b = \sqrt{3} \times a/2 = 4.906\,\text{Å}$ along $[1\bar{1}00]_M$ and $c = 4.531\,\text{Å}$ along $[0001]_M$.[7] The Mn+Sn layers alternate with the Mn-only layers along $[11\bar{2}0]_M$, and the double-sized unit cell for the Mn+Sn layer as shown by the faint orange-colored dashed rectangle.
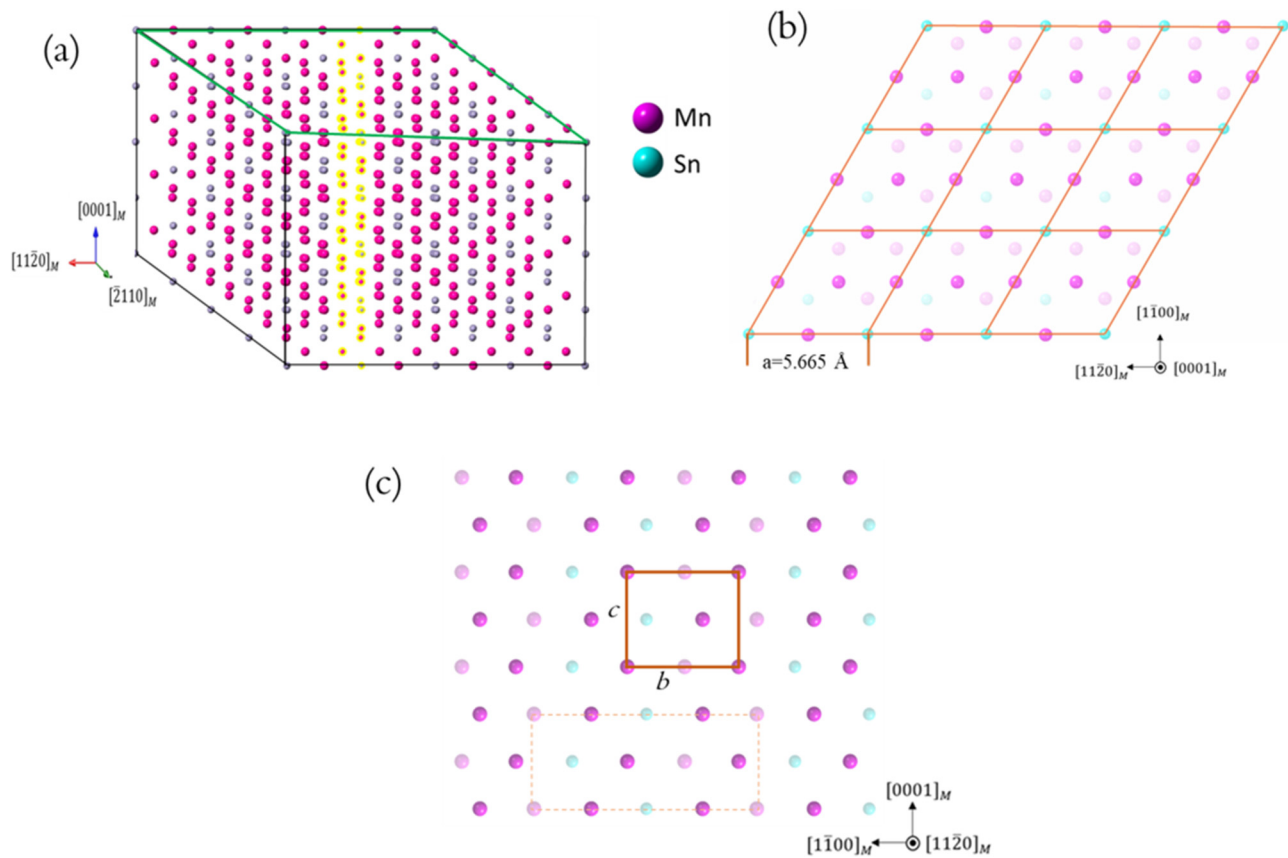
FIG. 1. (a) 3D model of Mn$_3$Sn indicating the *c*-plane in green color parallelogram as well as the cut (shown in yellow color) that was made to get the 2D *a*-plane model; (b) *c*-plane model. (c) Top view of the (bulk-like) 2D crystal model for the *a*-plane oriented sample. The magenta spots show the Mn atoms in the first layer, and the faded magenta and cyan spots indicate the Mn and Sn atoms, respectively, in the second layer. Figure generated using CrystalMaker®.[27]

Oh *et al.* grew Mn$_3$Sn on *m*-plane sapphire by first growing a low-temperature buffer layer of Mn$_3$Sn using sputter deposition, reporting an *a*-plane oriented poly-crystalline Mn$_3$Sn film.[6] Bai *et al.* reported the size-dependent AHE in a (11$\bar{2}$0) oriented Mn$_3$Sn film, where the coercive field of the AHE decreased abruptly when the width of the Hall bar was decreased to hundreds of nanometers.[8] The reason for this coercivity variation is explained to be due to the transition from multidomain to a single domain-like mode and from the reduction of the Néel temperature. Furthermore, Zhou *et al.* reported the presence of exchange bias which is generally observed in ferromagnet/antiferromagnet bilayer films, in a (11$\bar{2}$0) oriented Mn$_3$Sn film after field cooling. The exchange bias was attributed to the frozen antiferromagnetic part pinning the weak moments.[9]

On the other hand, the application of strain causes dramatic changes in the physical properties of magnets; it can modulate the magnetic anisotropy, tune magnetic transition temperatures, and control multiferroic properties.[10,11] The strain dependence of the magnetization most commonly comes in the form of magnetostriction, piezomagnetism, or flexomagnetism.[12] The non-collinear antiferromagnetic configuration of Mn$_3$Sn is the source of several anomalous transport properties including giant anomalous Hall,[13,14] Nernst,[15,16] magneto-optical Kerr,[17] and magnetic spin Hall effects.[18] These quantities were recently shown to be strongly strain-dependent. For example, Ikhlas *et al.* switched the sign of the Hall coefficient in Mn$_3$Sn by applying uniaxial strain.[19] Recently, Higo *et al.* found that only 0.2% strain along [21$\bar{1}$0] was enough to cause uniaxial magnetic anisotropy normal to the *c*-plane. This enabled 100% electrical switching of the perpendicularly oriented magnetic octupole confined within the Kagome plane, shown by AHE readouts with a small critical current density less than 15 MA/cm^2.[20] This result indicates that the strain of the film can be key for transport properties along with the crystal orientation.

We synthesize crystalline Mn$_3$Sn films using molecular beam epitaxy (MBE) in this work. The material is deposited without buffer layers on *c*-plane sapphire substrates and monitored both *in situ*, using reflection high energy electron diffraction (RHEED), and *ex situ* using x-ray diffraction (XRD), scanning transmission electron microscopy (STEM), Rutherford backscattering (RBS), and

other measurements. Our results for the samples grown at $453 \pm 5\,°C$ gave us a mixed orientation sample with the highest fraction being a-plane oriented Mn_3Sn and the next highest fraction being c-plane oriented Mn_3Sn, making this important to study in detail. We discuss the epitaxial film-substrate orientation relationships as well as the effect of strain in the samples. We compare these results to the theoretical atomic models to explain the most stable configuration depending on the orientation of Mn_3Sn lattice on high symmetry sites of the $Al_2O_3(0001)$ substrate.

II. EXPERIMENTAL

The samples were deposited in a custom-designed ultra-high vacuum (UHV) MBE chamber equipped with Mn and Sn effusion cells (SVT Associates), a quartz-crystal thickness monitor (Inficon STM-2 with an internal crystal oscillator), and a RHEED system (STAIB Instruments). The chamber vacuum is maintained with a base pressure in the 10^{-8}–10^{-9} Torr range using a UHV Cryoplex 8 cryopump on a 10-in. CF flange (Trillium). The RHEED data are acquired using a RHEED data acquisition system (k-Space Associates, Inc.). Crystalline Mn_3Sn films were deposited on commercially available Al_2O_3 (0001) substrates, with a single side polished grown by the Czochralski method and having a miscut of $\pm 1/2$ deg and surface roughness $R_A < 5\,Å$ (MTI Corporation). The (0001) substrates are cleaned using solvents (acetone and isopropanol) in an ultrasonicator and then mounted on 3-in. bayonet-style sample blocks and introduced into the MBE chamber where they are annealed at $770\,°C$ for 60 min on a custom MBE growth stage having a graphitic heater and built-in thermocouple (SVT Associates). The temperature (read out by a Eurotherm 2416 temperature controller) was calibrated using a Fluke single color pyrometer (model number E2MH-F0-V-0-0), focus range of 7.512 in., using a wavelength of $1.6\,\mu m$, with emissivity set at 0.7 and viewport transmissibility set at 0.93 based off of values published by Lesker.[21] After annealing, the substrate temperature is lowered to the deposition temperature.

Before every experiment, the source fluxes were checked using the *in situ* quartz crystal thickness monitor (TM) to determine the ratio of Mn:Sn used for the experiment. The sample was deposited at $453 \pm 5\,°C$ for 90 min, which ideally gives ~ 200 nm thick films. The film deposition is monitored using RHEED with an incident electron beam energy of 20 keV, providing information on crystalline quality and the *in-plane* lattice parameter. Once the sample is removed from the MBE chamber, it is investigated using XRD to determine the crystal structure and *out-of-plane* lattice parameter. To confirm the thickness and composition of the grown films, we used RBS.

A Thermo-Fisher Xe plasma G4 dual-beam focused ion beam (FIB) was used for *in situ* FIB lift-out preparation for the transmission electron microscopy (TEM) study with the final beam condition setting as 5 keV and 10 pA beam current to reduce the FIB damage. Those conditions were also used for SEM imaging. For element maps, Thermo-Fisher Talos F200 TEM with four 30 mm² SSD X-ray detectors attached was used and was operated in scanning transmission electron microscopy (STEM) and conventional TEM mode, respectively. A JEOL JEM-3100R05 with double aberration correctors was used for high-resolution STEM imaging, giving a spatial resolution better than 0.1 nm. When operated in

STEM mode using the two TEMs, high-angle annular dark-field (HAADF), low-angle annular dark-field (LAADF), and bright-field images were collected simultaneously.

III. THEORETICAL METHODOLOGY

First principles calculations were carried out using the projector augmented wave (PAW) method[22] in the framework of density functional theory (DFT), as implemented in the Vienna ab initio simulation package (VASP).[23] The exchange-correlation effects were treated within the generalized gradient approximation (GGA) parameterized by the Perdew–Burke–Ernzerhof (PBE) exchange-correlation functional.[24] The electronic configuration of Al, O, Mn, and Sn atoms are $3s^2\,3p^1$, $2s^2\,2p^4$, $3p^6\,4s^2\,3d^5$, and $5s^2\,5p^2$, respectively. A plane wave cut-off energy of 520 eV and a supercell having 2×2 periodicity for sapphire have been used. A vacuum layer of $15\,Å$ was used to eliminate the interaction between the periodically repeated slabs. The Brillouin zone integration has been done using a special k-point grid of $5 \times 5 \times 1$ for the structural optimization of the sapphire (0001) surface. The convergence criteria of energy and force calculations are set to 10^{-6} eV/atom and 0.01 eV/Å. Due to the non-collinear nature of Mn_3Sn, spin–orbit coupling was employed for all calculations. For the calculated equilibrium lattice constants of bulk Mn_3Sn, we have found $a = 5.59\,Å$, $c = 4.44\,Å$, and $m_{Mn} = 2.9\,\mu_B$. These values are in good agreement with previous GGA calculations finding $a = 5.57\,Å$ and $c = 4.43\,Å$.[25] Our results are slightly lower than the experimental values $a = 5.656\,Å$, $c = 4.531\,Å$, and $m_{Mn} = 3\mu_B$.[7]

IV. RESULTS

A. Experimental results

We deposited Mn_3Sn thin films on $Al_2O_3(0001)$ substrates at a growth temperature of $453 \pm 5\,°C$. The Mn and Sn fluxes were set to values of 1.6×10^{14} and 4.9×10^{13} atoms/cm² s, respectively, giving a flux ratio $J_{Mn}/J_{Sn} = 3.3$ which was used for this growth. The RHEED evolution is shown in Fig. 2.

Figures 2(a) and 2(b) show the RHEED patterns of annealed Al_2O_3 prior to the beginning of the deposition. Note that the black arrows shown in Fig. 2(b) highlight the Kikuchi lines that show up as additional peaks in the $[10\bar{1}0]_S$ line profile. The patterns became dim streaks and spotty, as shown in Figs. 2(c) and 2(d), immediately after opening shutters, and after 15 min of deposition, respectively. After 90 min, the RHEED pattern mostly or completely vanished, as shown in Figs. 2(e) and 2(f). This may indicate a high degree of surface atom mobility within the top surface layers. However, the RHEED patterns reappeared the next day at 300 K, as shown in Figs. 2(g) and 2(h).

After the surface is crystallized, the RHEED patterns show a combination of well-ordered point and spot pattern in both directions. The main point to observe is that the RHEED patterns follow the sapphire pattern very closely which in the case of the c-plane growth would not be true. As shown in Fig. 1(b), the *in-plane* spacing of c-plane Mn_3Sn is larger as compared to sapphire *in-plane* spacing ($a_M = 5.665\,Å$ vs $a_S = 4.759\,Å$) which would lead to a more closely spaced reciprocal space spots which is in contrast to what is observed in Figs. 2(i) and 2(j). On the other hand,

considering the *a*-plane model shown in Fig. 1(c), the reciprocal spacing would be closely following sapphire because the *in-plane* spacing is better than the *c*-plane lattice mismatch ($b_M = 4.960$ Å vs $a_S = 4.759$ Å and $c_M = 4.531$ Å vs $a_S = 4.759$ Å) as seen in Figs. 2(i) and 2(j). The spots seen in Figs. 2(h) and 2(j) (indicated by blue circles) are ascribed to misoriented grains as opposed to well-oriented grains and can be eliminated using an alternate growth technique; as such, we will not discuss these blue-circled

spots further. Instead, we focus on the point RHEED patterns, which are faint but visible in Figs. 2(i) and 2(j). These point patterns indicate an island growth mode as observed in both azimuthal directions. From these point patterns, the *in-plane* lattice spacings can be calculated by taking line profiles across Figs. 2(a) and 2(b) and across Figs. 2(i) and 2(j) for sapphire and Mn₃Sn, respectively, as shown in Fig. 3.

For $[11\bar{2}0]_S$, the primary streak spacing of Mn₃Sn is slightly wider as compared to the sapphire as observed in Fig. 3(a). In this case, the reciprocal spacing for sapphire is $4\pi/\sqrt{3}a_S$, while the reciprocal spacing for Mn₃Sn is $2\pi/a_{1,M}$. The ratio of these is the RHEED streak spacing ratio which can be used to solve for the Mn₃Sn lattice parameter with the following formula:

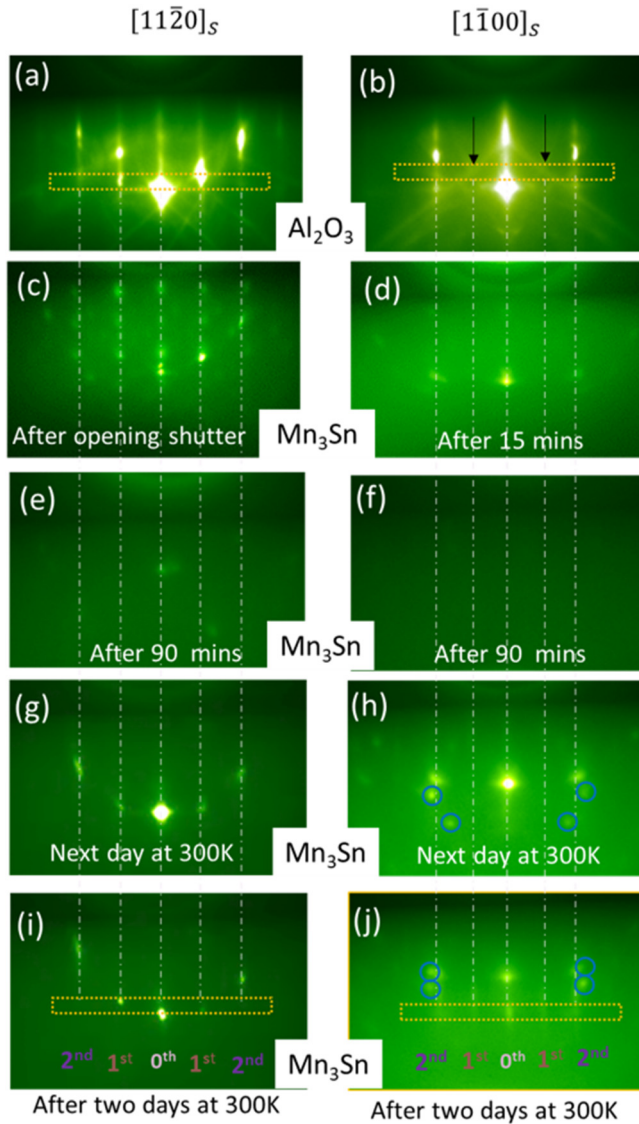$$a_{1,M} = a_S \times \frac{\sqrt{3}}{2} \times \frac{W_S}{W_M}. \tag{1}$$

FIG. 2. RHEED patterns of Al₂O₃ and growth of Mn₃Sn are shown where the yellow boxes show the positions where line profiles are taken and the dotted–dashed lines indicate the positions of the sapphire streaks. (a) and (b) annealed Al₂O₃; (c) immediately after opening Mn and Sn shutter simultaneously at 453 °C; (d) after 15 min of growth; (e) and (f) after 90 min of growth; (g) and (h) Mn₃Sn the next day at 300 K; (i) and (j) Mn₃Sn after 2 days at 300 K.
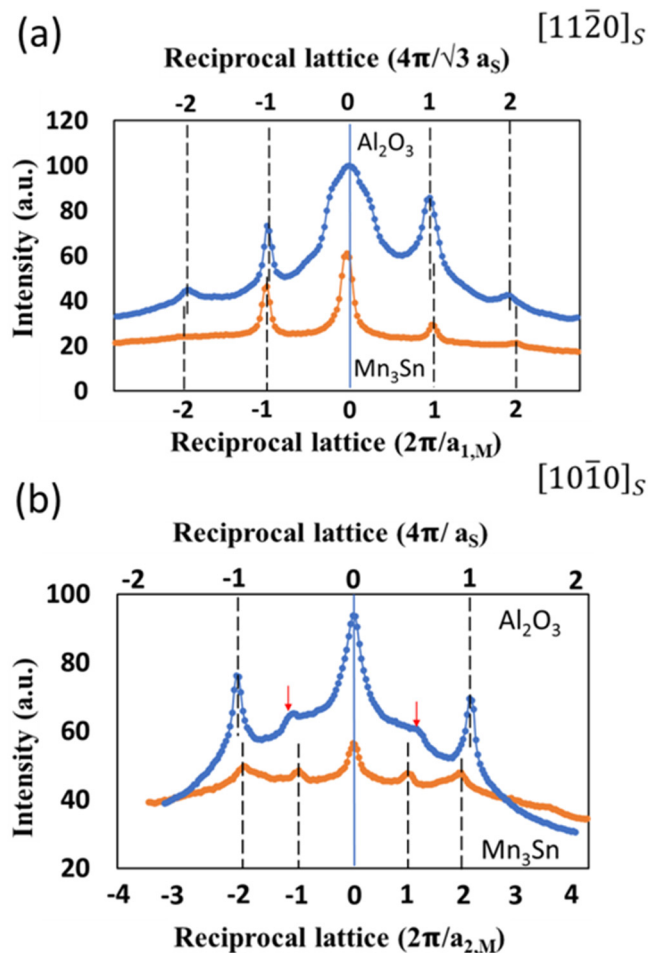

FIG. 3. Line profiles of the RHEED patterns for annealed Al₂O₃ and Mn₃Sn in (a) $[11\bar{2}0]_S$ and (b) $[10\bar{1}0]_S$ directions. Red arrows indicate Kikuchi lines for sapphire.
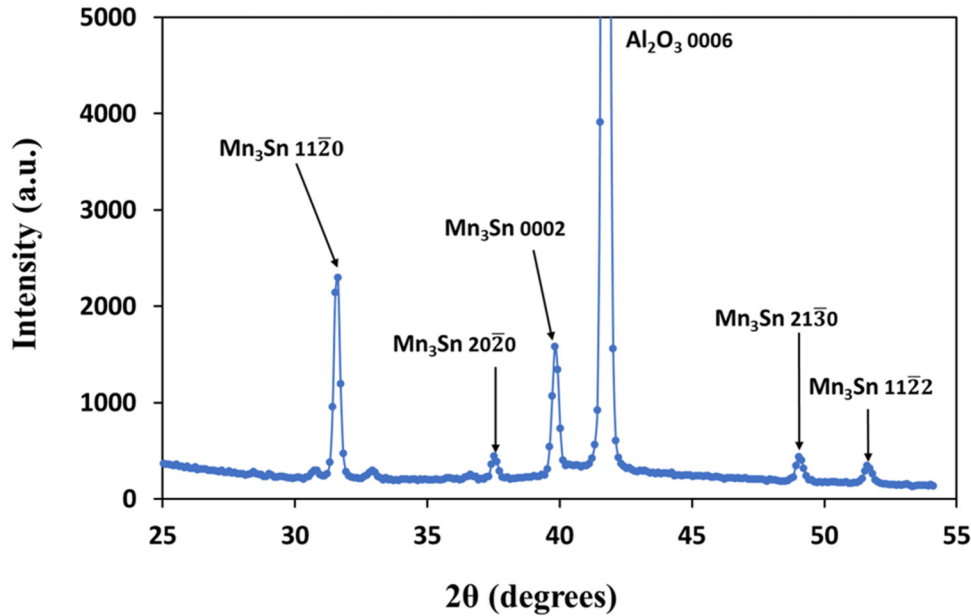
27 August 2023 17:26:23

FIG. 4. X-ray diffraction pattern of $Mn_3Sn/Al_2O_3(0001)$ grown at 453 °C at a Mn:Sn flux ratio of 3.3:1.

Using this equation, the lattice parameter along $[11\bar{2}0]_S$ is calculated to be $a_{1,M} = 4.117 \pm 0.027$ Å (note: we use the term "lattice parameter" instead of lattice constant to avoid confusion with the a and c values of Mn_3Sn).

For $[10\bar{1}0]_S$, the Mn_3Sn streaks are quite weak and the second order streak spacing is slightly smaller compared to Al_2O_3 first-order streaks, as seen in Fig. 3(b). In this case, the reciprocal spacing for sapphire is $4\pi/a_S$ while the reciprocal spacing for Mn_3Sn is $2\pi/a_{2,M}$. Therefore, using the second-order Mn_3Sn streaks, the RHEED streak spacing ratio will be equal to $(4\pi/a_S)/(2 \times 2\pi)/a_{2,M})$ which can be solved for the Mn_3Sn lattice parameter as in the following equation:

$$a_{2,M}, = a_S \times \frac{W_S}{W_M}. \qquad (2)$$

This leads to the lattice parameter along $[10\bar{1}0]_S$, $a_{2,M} = 4.943 \pm 0.033$ Å.

In order to further understand the presence of these spots and point pattern observed in RHEED, we carried out XRD as shown in Fig. 4. For the substrate, the diffraction peak at 41.72° is the Al_2O_3 0006 peak which gives a d-spacing of 2.165 Å, corresponding to the known value for $c_S = 12.991$ Å at 300 K. The Mn_3Sn 0002 peak at 39.82° gives a value of $c_M = 4.528 \pm 0.014$ Å. This value is in very good agreement with the c_M value reported by Higo et al.[26] (4.531 Å) (a difference of only −0.06%). This c-oriented component of the sample is 30% of the total summed Mn_3Sn peak intensities.

The $11\bar{2}0$ Mn_3Sn peak at 31.62° gives a lattice parameter of 5.660 $\pm$ 0.018 Å corresponding to a_M and corresponds to 46% of the total summed Mn_3Sn peak intensities. The XRD value (5.660 Å) is −0.08%

away from the a_M value reported by Higo et al.[26] (5.665 Å). The XRD also shows the presence of several other orientations, including the Mn_3Sn $20\bar{2}0$, $21\bar{3}0$, $11\bar{2}2$ and Mn_2Sn 0002, which all have significantly smaller intensities compared to the $11\bar{2}0$ peak. The intensities for all the peaks are given in Table I. Hence, XRD indicates a polycrystalline film with largest percentage of $11\bar{2}0$ peak and in order to study the surface and interface, SEM and STEM were carried out.

Figure 5 shows an SEM image of the sample where it appears that the sample is discontiguous. The individual islands are clearly
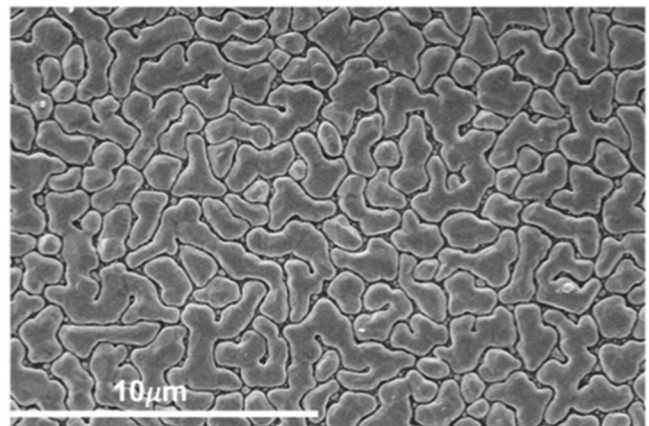

FIG. 5. SEM image showing the morphology of the sample which was grown at 453 °C with flux ratio Mn: Sn = 3.3:1.

distinct, giving the morphology a labyrinthine appearance. The scale bar is shown, and it is seen that the characteristic island width is only about 1 μm. On the other hand, some islands meander for many micrometers from one end to the other.

Furthermore, cross-sectional STEM was carried out to understand the interface as well as the surface of the film and elemental composition of the film. Figures 6(a) and 6(b) are the STEM images, using bright field and dark field, respectively, showing large variations in the island widths of up to ~1600 nm (which agrees with the SEM image data) and island heights of ~200 nm.

Additionally, Figs. 6(c) and 6(d) show the elemental composition of Al and O, respectively, which maps out the sapphire substrate. Some oxygen is also seen at the surface of the film. Figures 6(e) and 6(f) show the elemental composition of Mn and Sn, where the constant color contrast across the islands indicates a uniform composition. RBS was also carried out to determine the composition of the sample, giving a ratio for Mn:Sn = 3.26:1, and the RBS thickness of the film was calculated to be ~220 nm, which agrees well with the STEM data shown in Fig. 6. The STEM images further confirm an island growth mode (which agrees with RHEED) with a film that is not smooth overall. The crystalline quality is further investigated by carrying out lattice imaging.

Figure 7(a) shows the lattice imaging of the Mn_3Sn film. Here, we see a clear hexagonal lattice corresponding to the c-plane, and shown in Fig. 7(b) is a c-plane model for comparison which is of a single layer of the Mn_3Sn lattice. The Mn and Sn atoms are represented with magenta and cyan colored balls, respectively, and a yellow hexagon is drawn to compare to the hexagon shown in the STEM image shown in Fig. 7(a). By comparison of the model with the STEM image, we can identify the bright spots of the image as the Sn-atoms in the model.

The scale of the image in Fig. 7(a) was calibrated by using the STEM image of the sapphire substrate along the $[11\bar{2}0]_S$ axis. Then the in-$plane$ (x axis) spacing between bright spots is measured to be 4.960 $\pm$ 0.03 Å which, comparing to the expected $b = 4.906$ Å, is larger by +1.10%. This could be interpreted as either due to an in-$plane$ tensile strain or to a difference in stoichiometry [our sample measured 3.26:1 (Mn to Sn) vs the ideal 3:1].

Similarly, the y axis spacing in the STEM image was measured to be 5.653 $\pm$ 0.03 Å which compared to the calculated XRD ($a_M = 5.660$ Å), is smaller but only by -0.12%, showing the accuracy of the STEM measurements, and as compared to the expected 5.665 Å, is smaller but only by -0.21%. This could also be interpreted as either due to an out-of-$plane$ compressive strain or to the difference in stoichiometry. However, since the in-$plane$ and out-of-$plane$ values should be proportional in the case of the deviations being due to stoichiometry, whereas they give opposite deviations from expected values, it seems more likely to be strain related.

Figure 7(c) shows the interface between Mn_3Sn and Al_2O_3 (0001) which indicates disordered zone (orange line) extending about ~8.5 Å from the sapphire interface. This disordered region may allow the crystal structure to relax to its near bulk value along the $[1\bar{1}00]_S$, which from STEM is measured to be 4.960 Å which compared to the measured RHEED value of 4.943 Å is consistent within the error bar. Calculating an effective a_M in-$plane$ value of 4.960 Å $\times$ $2/\sqrt{3} = 5.727$ Å, and taking a ratio to the out-of-$plane$ value of 5.653 Å, we determine a hexagonal distortion within the upright c-plane of 1.31%.

Assuming these are strain values, we can calculate a Poisson's ratio, defined from the formula $v = (in$-$plane\ strain)/(out$-of-$plane\ strain)$, resulting in $v = -5.2$. Also, from the model, we see that the lattice is oriented with $[11\bar{2}0]_M$ (the $\vec{a}$ direction) being along

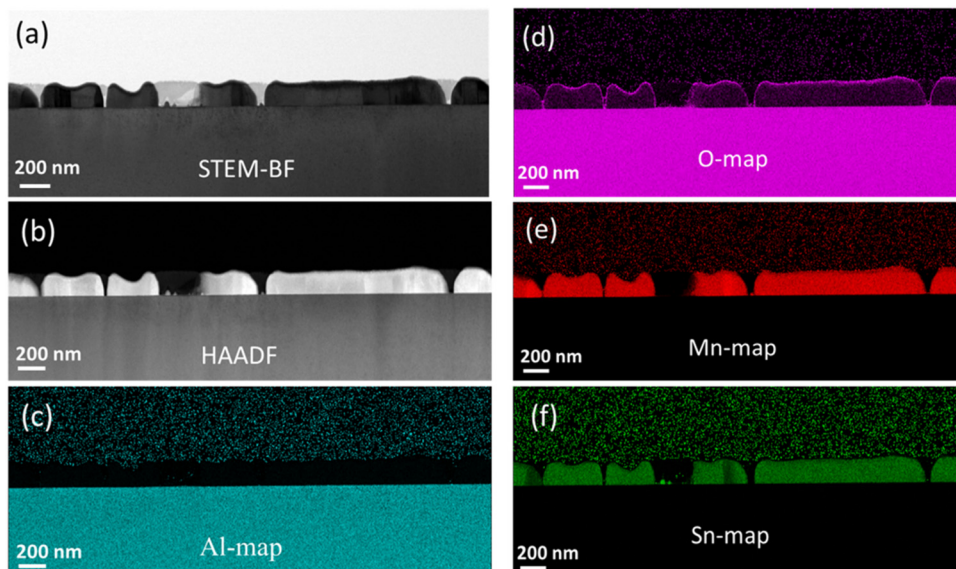<div style="writing-mode: vertical;">27 August 2023 17:26:23</div>

FIG. 6. Elemental analysis indicating the composition of Mn and Sn for the sample. (a) Bright-field image; (b) HAADF image; (c)–(f) Al-, O-, Mn-, and Sn-maps showing the distribution of elements in the film.
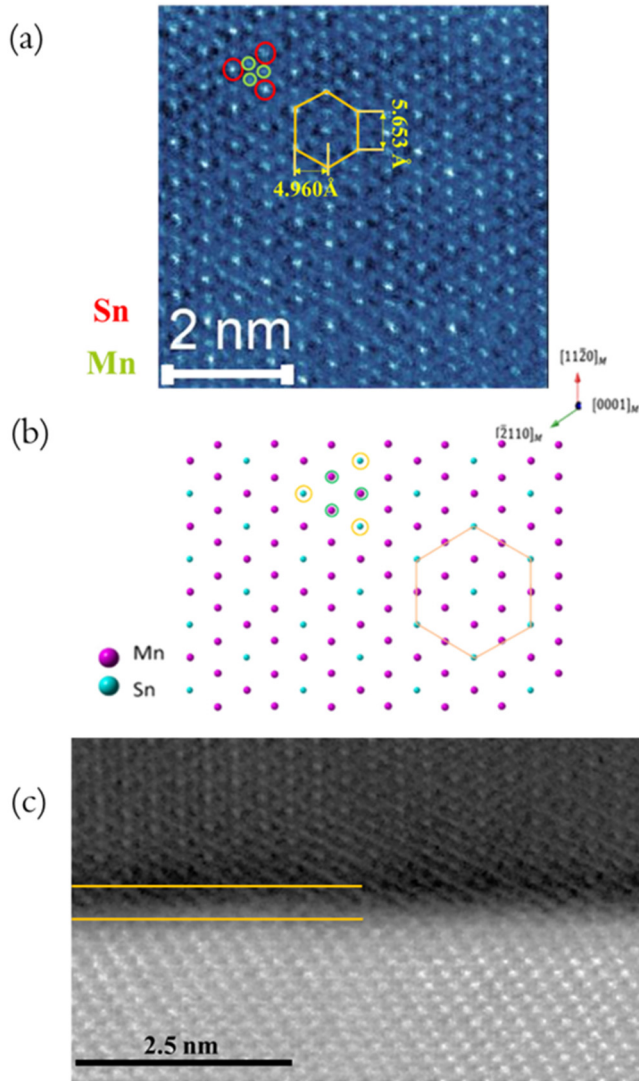
FIG. 7. Lattice imaging showing (a) the presence of Mn and Sn by green (small) and red (large) circles, respectively. The numbers shown in the image were calculated for Mn_3Sn after calibrating the STEM image scale using the sapphire lattice image and the well-known LC of sapphire. (b) STEM model corresponding to the lattice image matching the positions of Mn (magenta dots, small cyan circled) and Sn (cyan dots, large yellow circled. Sn atoms at the vertices of the hexagon. Figure generated using CrystalMaker®.[27] (c) Interface between sapphire and grown Mn_3Sn.

FIG. 8. Overlay of the Mn_3Sn a-plane on c-plane (0001) Al_2O_3 is shown for two cases (a) $[0001]_M \parallel [11\bar{2}0]_S$; (b) $[0001]_M \parallel [1\bar{1}00]_S$. Magenta-colored circles (solid circles at vertices of dotted rectangular lattice) indicate Mn atoms, and cyan-colored circles (solid circles at edge centers of dotted rectangular lattice) indicate Sn atoms.

the y axis. Therefore, the STEM lattice image confirms the presence of a-plane orientation. Based on RHEED, XRD, and STEM, we next discuss the epitaxial relationship of the film with the sapphire substrate.

Figure 8 shows two possible epitaxial orientations of the Mn_3Sn lattice overlaid on top of c-plane sapphire (0001). Options (a) and (b) arise naturally because the hexagonal sapphire lattice
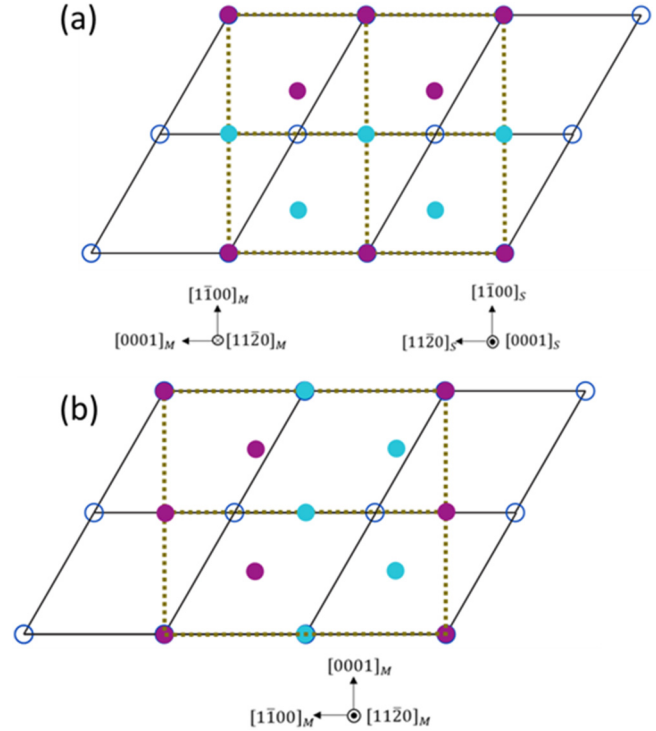
can be viewed as having an unconventional rectangular lattice with unit cell (4.759 Å along $\mathbf{a_S}$) × (8.242 Å along $\mathbf{b_S}$).

We note that although the XRD spectrum shows a strong $11\bar{2}0$ a-plane peak, giving a lattice parameter of 5.6508 Å, the RHEED patterns do not agree especially well with the rectangular lattice expected for an a-plane orientation. If one has a hexagonal substrate, then placing a rectangular lattice on top should result in at least 3 (if not 6) different rotated orientations. And yet the RHEED patterns do not show multiple streak spacings nor ring-like, polycrystalline streaks as might be expected. Furthermore, none of the obtained lattice parameters from RHEED match the expected a-plane bulk values, even after trying various rotations. This could imply that a significant amount of in-plane strain exists within the sample. In the following, we consider the two possible orientations in turn, discussing the lattice mismatch and the strain from the Mn_3Sn bulk values in each case.

Figure 8(a) shows a model that is consistent with the STEM lattice image measurements as seen in Fig. 7(a). In this orientation, the $\mathbf{c_M}$ axis = $[0001]_M$ is aligned with $\mathbf{a_S}$ = $[11\bar{2}0]_S$. With this orientation, $\mathbf{a_M} \parallel \mathbf{c_S}$; $\mathbf{b_M} \parallel \mathbf{b_S}$; $\mathbf{c_M} \parallel \mathbf{a_S}$, and in terms of expected mismatch with the substrate, $2 \times b_M$ (4.906 Å) is a +19.0% mismatch compared to $2 \times b_S$ (4.121 Å), but c_M (4.531 Å) is only a −4.79%

TABLE I. Summary of the RHEED, XRD, and RBS results of the sample deposited at $453 \pm 5\,^{\circ}$C.

XRD				RHEED	RBS	STEM
2θ	Peak label	Relative intensities	Lattice parameter	Average lattice parameter	Composition and thickness	Lattice parameters
31.62	Mn_3Sn $11\bar{2}0$	43%				*in-plane*
33.02	Mn_2Sn 0002	5%	Mn_3Sn $11\bar{2}0$:	$a_{1,M}$:	Mn:Sn:	b_M:
37.52	Mn_3Sn $20\bar{2}0$	7%	a_M: 5.660 ± 0.018 Å	4.117 ± 0.027 Å	3.26:1	4.960 ± 0.03 Å
39.82	Mn_3Sn 0002	30%	Mn_3Sn 0002:	$a_{2,M}$:	Thickness	*out-of-plane*
49.12	Mn_3Sn $21\bar{3}0$	8%	c_M: 4.528 ± 0.014 Å	4.943 ± 0.033 Å	~220 nm	a_M:
51.72	Mn_3Sn $11\bar{2}2$	6%				5.653 ± 0.03 Å

mismatch compared to a_S (4.759 Å). In terms of possible strain within the film from our measurements, in this orientation the $\mathbf{b_M}$ axis is under $+1.10\%$ tensile strain (4.960 Å measured by STEM compared to 4.906 Å unstrained, Tomita *et al.*) while the $\mathbf{c_M}$-axis would be under $+9.09\%$ tensile strain (4.943 Å measured by RHEED vs 4.531 Å unstrained, Tomita *et al.*).[7]

Figure 8(b) shows the orientation that matches better with the RHEED data. This orientation is just rotated 90° with respect to the first orientation model around the $\mathbf{a_M}$ axis such that $\mathbf{b_M} \parallel \mathbf{a_S}$ and $\mathbf{c_M} \parallel \mathbf{b_S}$. In terms of the expected lattice mismatch, b_M (4.906 Å) has a $+3.09\%$ mismatch compared to a_S (4.759 Å), while c_M (4.531 Å) has a $+9.95\%$ mismatch compared to b_S (4.121 Å). But in terms of possible strain in this orientation, the $\mathbf{b_M}$ axis is under a tensile strain of $+0.75\%$ by comparison of the measured b_M (4.943 Å) from RHEED to the ideal b_M (4.906 Å) from Tomita *et al.*'s value for a_M (5.665 Å), while the $\mathbf{c_M}$ axis is under a compressive strain of -9.14% from comparing the measured c_M (4.117 Å) from RHEED with the ideal c_M (4.531 Å from Tomita *et al.*).[7] The large strain in this orientation may, however, indicate a coincidence lattice matching with the sapphire substrate lattice along $\mathbf{b_S}$ given that $2\times$ the measured c_M equals 8.234 Å and $2\times$ the substrate lattice spacing b_S equals 8.242 Å, corresponding to a difference of only -0.097% and along b_M the lattice mismatch with the substrate is $+3.866\%$ (4.943 Å vs 4.759 Å). Table I summarizes the XRD, RHEED, and RBS results. In this table are listed: 2θ, corresponding peak labels, and relative XRD peak intensities, plus lattice parameters from XRD and RHEED and composition from RBS. Clearly, the sample contains mixed orientations but with the largest percentage from the $11\bar{2}0$ peak.

B. Theoretical results

Taking into account the models shown in Figs. 8(a) and 8(b), first principle calculations were performed to determine the most stable model of Mn_3Sn formation on the $(0001)_S$ surface. For this aim, we have only considered the high symmetry sites (L2, L3, H3, and T4) of $(0001)_S$. Figure 9 illustrates the high symmetry sites. In

the L2 site, the Mn adatom is placed on top of a second layer Al atom. For the L3 site, the Mn adatom is placed on top of a third layer Al atom. For the T4 site, the Mn adatom is placed on top of the first layer O atom. And finally, for the H3 site, the Mn adatom is placed on top of a second layer O atom.
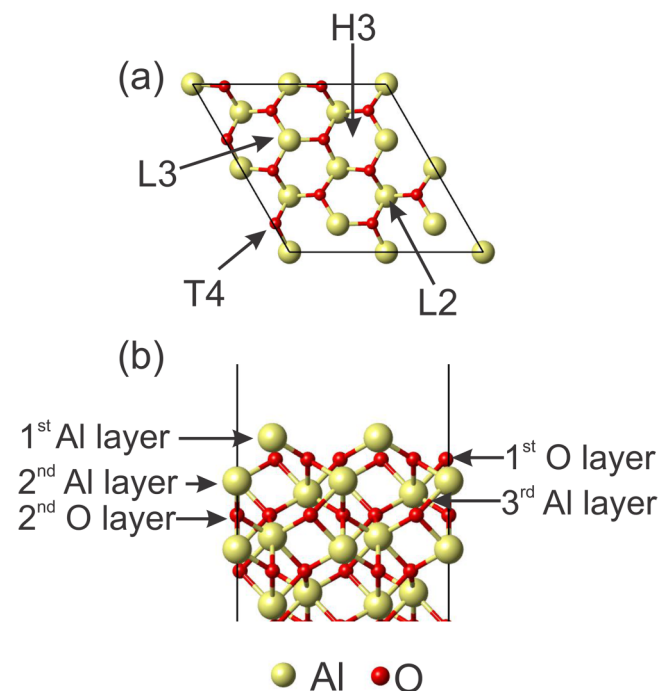

FIG. 9. Schematic atomic structure for a $(0001)_S$-(2×2) unit cell, showing the high symmetry sites: L2, L3, H3, and T4. The model shown in (a) is for the top view and in (b) is for the side view.
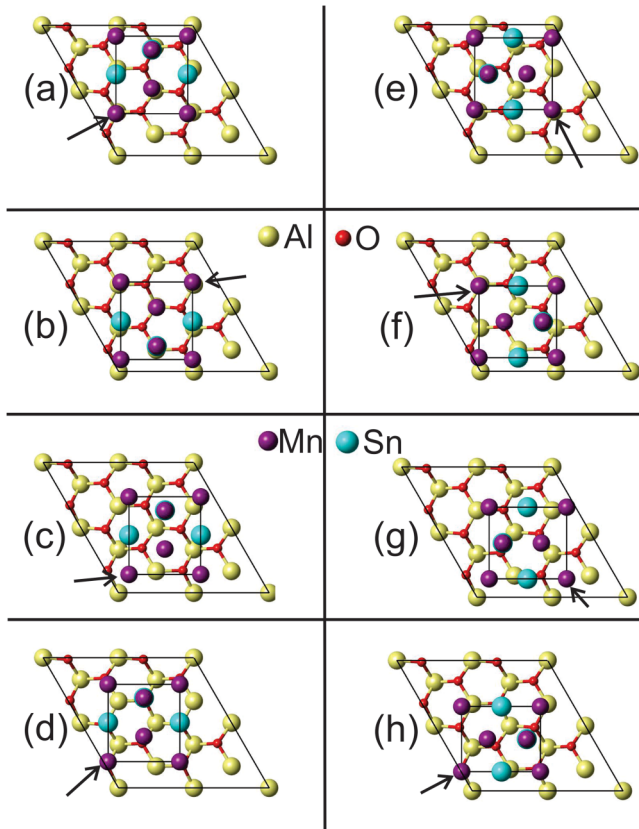
27 August 2023 17:26:23

FIG. 10. Top view of atomic models for the a-plane Mn_3Sn on $(0001)_S$. Panels (a)–(d) represent the Mn_3Sn lattice unit cells models corresponding to L2, L3, H3 and T4 sites, respectively, with $c_M \parallel a_S$. Panels (e)–(h) represent the 90° rotated Mn_3Sn such that $c_M \parallel b_S$ on L2-R90°, L3-R90°, H3-R90°, and T4-R90° sites, respectively. The black arrows show the Mn adatom sites used for these model calculations.

Since $[11\bar{2}0]_M$ exhibits a rectangular unit cell, we have chosen the Mn corner atom as the reference point for these calculations as indicated by the black arrows in Fig. 10. Figures 10(a)–10(d) display the a-plane Mn_3Sn lattice unit cell on the four different high symmetry sites corresponding to the schematic model shown in Fig. 8(a) having $c_M \parallel a_S$. In addition, the Mn_3Sn lattice was rotated 90° along the anticlockwise direction to produce four R90°

TABLE II. Relative energies for different high symmetry sites for $[11\bar{2}0]_M$ on $(0001)_S$. Zero energy (bold numbers) represents the most stable configuration.

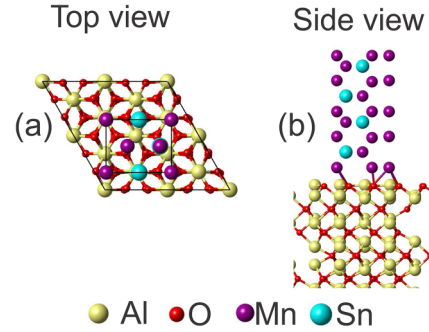| Models	Energy (eV)	Models	Energy (eV)
L2	4.09	L2-90°	4.74
L3	0.67	**L3-90°**	**0.00**
H3	1.09	H3-90°	3.55
T4	1.02	T4-90°	2.62

FIG. 11. Schematic atomic model of $(11\bar{2}0)_M$ on $(0001)_S$. (a) Top view and (b) side view.

models having $c_M \parallel b_S$, as shown in Figs. 10(e)–10(h), corresponding to the schematic Mn_3Sn model shown in Fig. 8(b).

In order to compare the various models, we report the relative energies in Table II, where the bold numbers correspond to the reference energy. According to the energetic calculations and structural optimization, the L2 and L2-R90° models are very high in energy, implying that these are unstable configurations. Similarly, H3, H3-R90°, T4, and T4-R90° are also high in energy. The most stable models corresponds to the L3 and L3-R90°, with L3-R90° being the lowest in energy. In addition, the Mn_3Sn lattice constants for the most stable model were: $b_M = 4.96$ Å and $c_M = 4.02$ Å, implying a tensile strain of +1.43% (compared to our equilibrium, bulk value $b_M = 4.89$ Å) and a compressive strain of −9.46% (compared to our equilibrium, bulk value $c_M = 4.44$ Å), respectively.

These theoretical lattice parameters and strain values for Mn_3Sn growth on sapphire (0001) are in good agreement with our experimentally measured lattice parameters and strains based on RHEED. Compare b_M of 4.96 Å (theory) vs b_M of 4.943 Å (expt) and a calculated tensile strain of +1.43% (theory) vs +0.75% (expt). And compare a c_M of 4.02 Å (theory) with a c_M of 4.117 Å (expt) and a strain of −9.46% (theory) with −9.14% (expt).

From the theoretical calculations, we developed Fig. 11 showing an atomic model of Mn_3Sn $(11\bar{2}0)_M$ on Al_2O_3 $(0001)_S$. Figures 11(a) and 11(b) show the top and side views of the psuedomorphic overlay of Mn_3Sn on Al_2O_3, respectively. The measured strain from the RHEED is best seen from this model, which shows the coupling between the Mn atoms and the O atoms of the first layer. The covalent Mn–O bonds are stronger than the metallic bonds between the Mn and Al or Mn and Sn. In addition, Fig. 11(b) illustrates the above interface relationship mentioned: $[0001]_M \parallel [1\bar{1}00]_S$.

V. CONCLUSIONS

In conclusion, we performed the MBE growth of Mn_3Sn directly on c-plane sapphire (0001) substrates without buffer layers and have shown the material followed the substrate crystal lattice when grown at $453 \pm 5\,°C$. This growth procedure resulted in a mixed orientation with a higher percentage of $11\bar{2}0$ (a-plane). The *in-plane* and *out-of-plane* lattice parameters were calculated from RHEED, STEM, and XRD. The RHEED images showed the

presence of a point pattern indicative of an island growth mode which was further confirmed by the STEM images. Lattice parameters calculated from RHEED and STEM indicated an *in*-plane strain in the *a-plane* Mn_3Sn lattice. Lattice orientation models have been proposed to explain the experimental measurements. Different theoretical models were built to explain the growth of $(11\bar{2}0)_M$ on $(0001)_S$, where the L3-R90° model was found to be the most stable configuration which also agrees with the RHEED data.

We find that the RHEED data match best with the theoretically lowest energy L3-R90° model. On other hand, the STEM data agree with the L3 model, and the energy for this model from theory is not that much higher as compared to the L3-R90° model. It could be that the thermal energy of the sample made these two orientations both accessible in different parts of the sample.

These results should be interesting in light of the important finding by Higo *et al.* of perpendicular full switching in strained Kagome lattice Mn_3Sn thin films.[20] Our new findings of the strain effects which are possible to occur in *a*-plane oriented Mn_3Sn layers grown by MBE may lead to new discoveries in antiferromagnetic spintronics.

ACKNOWLEDGMENTS

AUTHOR DECLARATIONS

Conflict of Interest

The authors have no conflicts to disclose.

Author Contributions

Sneha Upadhyay: Conceptualization (equal); Data curation (equal); Formal analysis (equal); Investigation (equal); Methodology (equal); Resources (equal); Validation (equal); Visualization (equal); Writing – original draft (equal); Writing – review & editing (equal). **Tyler Erickson:** Conceptualization (supporting); Investigation (equal); Methodology (equal); Resources (equal); Writing – review & editing (supporting). **Hannah Hall:** Validation (supporting); Writing – review & editing (equal). **Ashok Shrestha:** Investigation (supporting); Methodology (supporting). **David C. Ingram:** Data curation (equal); Formal analysis (equal); Investigation (equal); Methodology (equal); Validation (supporting). **Kai Sun:** Data curation (equal); Formal analysis (equal); Investigation (equal); Methodology (equal); Validation (supporting). **Juan Carlos Moreno Hernandez:** Data curation (equal); Formal analysis (equal); Investigation (equal); Methodology (equal); Writing – original draft (equal); Writing – review & editing (equal). **Gregorio Hernandez Cocoletzi:** Formal analysis (supporting); Funding acquisition (supporting); Investigation (supporting); Methodology (equal); Resources (supporting); Supervision (equal); Validation (supporting); Writing – review & editing (equal). **Noboru Takeuchi:** Formal analysis (supporting); Funding acquisition (supporting); Investigation (supporting); Methodology (equal); Resources (equal); Software (equal); Supervision (equal); Validation (supporting); Writing – review & editing (equal). **Arthur R. Smith:** Conceptualization (equal); Data curation (equal); Formal analysis (equal); Funding acquisition (equal); Investigation (equal); Methodology (equal); Project administration (equal); Resources (equal); Software (equal); Supervision (equal); Validation (equal); Visualization (equal); Writing – original draft (equal); Writing – review & editing (equal).

DATA AVAILABILITY

The data that support the findings of this study are openly available in Zenodo at 10.5281/zenodo.7860078.

REFERENCES

[1] A. Markou, J. M. Taylor, A. Kalache, P. Werner, S. S. P. Parkin, and C. Felser, Phys. Rev. Mater. **2**, 051001(R) (2018).
[2] Z. Zhao, Q. Guo, F. Chen, K. Zhang, and Y. Jiang, Physica B **604**, 412692 (2021).
[3] S. Nakatsuji, N. Kiyohara, and T. Higo, Nature **527**, 212 (2015).
[4] J. M. Taylor, A. Markou, E. Lesne, P. K. Sivakumar, C. Luo, F. Radu, P. Werner, C. Felser, and S. S. P. Parkin, Phys. Rev. B **101**, 094404 (2020).
[5] J.-Y. Yoon, Y. Takeuchi, S. Dutta Gupta, Y. Yamane, S. Kanai, J. Ieda, H. Ohno, and S. Fukami, AIP Adv. **11**, 065318 (2021).
[6] S. Oh, T. Morita, T. Ikeda, M. Tsunoda, M. Oogane, and Y. Ando, AIP Adv. **9**, 035109 (2019).
[7] T. Tomita, M. Ikhlas, and S. Nakatsuji, JPS Conf. Proc. **30**, 011009 (2020).
[8] H. Bai, W. Zhu, Y. You, X. Chen, X. Zhou, F. Pan, and C. Song, Appl. Phys. Lett. **117**, 052404 (2020).
[9] X. F. Zhou *et al.*, Phys. Rev. Appl. **14**, 054037 (2020).
[10] R. Ramesh and N. A. Spaldin, Nat. Mater. **6**, 21 (2007).
[11] C. Song, B. Cui, F. Li, X. Zhou, and F. Pan, Prog. Mater. Sci. **87**, 33 (2017).
[12] F. Theuss, S. Ghosh, T. Chen, O. Tchernyshyov, S. Nakatsuji, and B. J. Ramshaw, Phys. Rev. B **105**, 174430 (2022).
[13] N. H. Sung, F. Ronning, J. D. Thompson, and E. D. Bauer, Appl. Phys. Lett. **112**, 132404 (2018).
[14] T. Ikeda, M. Tsunoda, M. Oogane, S. Oh, T. Morita, and Y. Ando, Appl. Phys. Lett. **113**, 222405 (2018).
[15] X. Li, L. Xu, L. Ding, J. Wang, M. Shen, X. Lu, Z. Zhu, and K. Behnia, Phys. Rev. Lett. **119**, 056601 (2017).
[16] H. Narita, M. Ikhlas, M. Kimata, A. A. Nugroho, S. Nakatsuji, and Y. Otani, Appl. Phys. Lett. **111**, 202404 (2017).
[17] T. Higo *et al.*, Nat. Photonics **12**, 73 (2018).
[18] M. Kimata *et al.*, Nature **565**, 627 (2019).
[19] M. Ikhlas, S. Dasgupta, F. Theuss, T. Higo, B. J. Ramshaw, O. Tchernyshyov, C. W. Hicks, and S. Nakatsuji, "Piezomagnetic switching of anomalous Hall effect in an antiferromagnet at room temperature," Nat. Phys. **18**, 1086–1093 (2022).
[20] T. Higo *et al.*, Nature **607**, 474 (2022).
[21] See https://www.lesker.com/viewports/viewports-cf-flanged-kodial-glass.cfm.

27 August 2023 17:26:23

[22]P. E. Blöchl, Phys. Rev. B **50**, 17953 (1994).

[23]G. Kresse and J. Furthmüller, Phys. Rev. B **54**, 11169 (1996).

[24]J. P. Perdew, K. Burke, and M. Ernzerhof, Phys. Rev. Lett. **77**, 3865 (1996).

[25]D. Zhang, B. Yan, S. C. Wu, J. Kübler, G. Kreiner, S. S. Parkin, and C. Felser, J. Condens. Matter Phys. **25**, 206006 (2013).

[26]T. Higo, D. Qu, Y. Li, C. L. Chien, Y. Otani, and S. Nakatsuji, Appl. Phys. Lett. **113**, 202402 (2018).

[27]Images and video generated using CrystalMaker®: A crystal and molecular structures program for Mac and Windows, CrystalMaker Software Ltd, Oxford, England, see www.crystalmaker.com.

27 August 2023 17:26:23